ADVANCED ENERGY MATERIALS

# Supporting Information

for *Adv. Energy Mater.*, DOI 10.1002/aenm.202401255

A Hybrid Biofuel Cell with High Power and Operational Stability Using Electron Transfer-Intensified Mediators and Multi-Interaction Assembly

*Younjun Jang, Tae-Won Seo, Junha Pak, Moon Kyu Park, Jeongyeon Ahn, Gee Chan Jin, Seung Woo Lee, Yoon Jang Chung*, Young-Bong Choi*, Cheong Hoon Kwon* and Jinhan Cho**

# Supporting Information

# A Hybrid Biofuel Cell with High Power and Operational Stability Using Electron Transfer-Intensified Mediators and Multi-Interaction Assembly

Younjun Jang[1], Tae-Won Seo[2], Junha Pak[1], Moon Kyu Park[3], Jeongyeon Ahn[3], Gee Chan Jin[4], Seung Woo Lee[5], Yoon Jang Chung[3]*, Young-Bong Choi[6]*, Cheong Hoon Kwon[4]*, and Jinhan Cho[1,3,7]*

[1]KU-KIST Graduate School of Converging Science & Technology, Korea University, 145 Anam-ro, Seongbuk-gu, Seoul 02841, Republic of Korea

[2]Department of Chemistry, College of Science & Technology, Dankook University, 119 Dandae-ro, Dongnam-gu, Cheonan-si, Chungcheongnam-do 31116, Republic of Korea

[3]Department of Chemical and Biological Engineering, Korea University, 145 Anam-ro, Seongbuk-gu, Seoul 02841, Republic of Korea

[4]Department of Energy Resources and Chemical Engineering, Kangwon National University, 346 Jungang-ro, Samcheok, 25913, Republic of Korea

[5]The George W. Woodruff School of Mechanical Engineering, Georgia Institute of Technology, Atlanta, Georgia 30332, USA

[6]Department of Cosmedical & Materials, Dankook University, 119 Dandae-ro, Dongnam-gu, Cheonan-si, Chungcheongnam-do 31116, Republic of Korea

[7]Soft Hybrid Materials Research Center, Advanced Materials Research Division, Korea Institute of Science and Technology (KIST), 5 Hwarang-ro 14-gil, Seongbuk-gu, Seoul 02792, Republic of Korea

*Address correspondence to yoonjang@korea.ac.kr, chem0404@dankook.ac.kr, chkwon2@kangwon.ac.kr, and jinhan71@korea.ac.kr

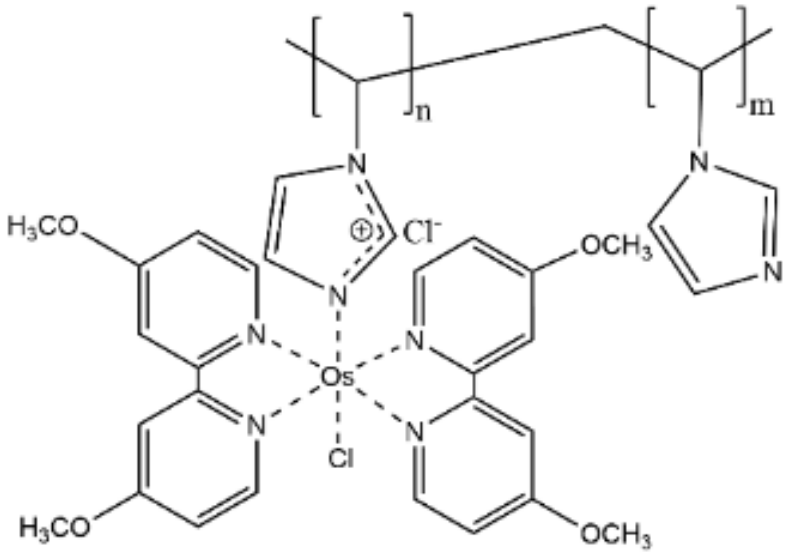


**Figure S1.** Molecular structure of Os-RM (i.e., poly(N-vinylimidazole)-[Os(4,4′-dimethoxy-2,2′-bipyridine)$_2$Cl])$^{+/2+}$).

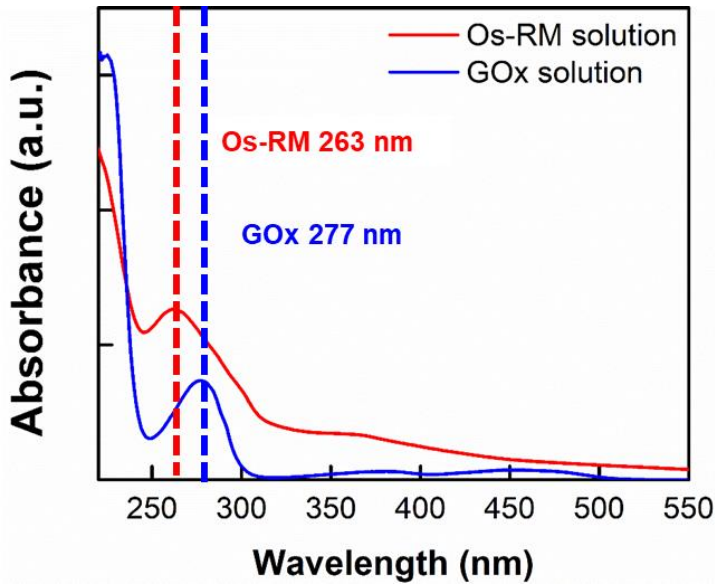


**Figure S2.** UV-vis spectra of Os-RM (peak at 263 nm) and GOx (peak at 277 nm) dispersed in a 20 mmol $L^{-1}$ PBS solution, respectively.

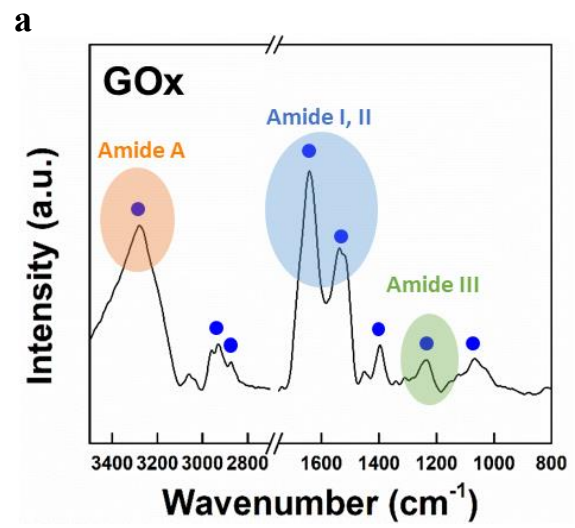


| Wavenumber ($cm^{-1}$) | Assignments |
|---|---|
| 3305 | Amide A |
| 2920 | C-H asymmetric stretching in $CH_2$ |
| 2856 | C-H symmetric stretching in $CH_3$ |
| 1640 | C=O stretching Amide I |
| 1539 | N-H stretching Amide II |
| 1378 | C-H bending $CH_3$ |
| 1213 | Amide III |
| 1110 | C-O stretching |

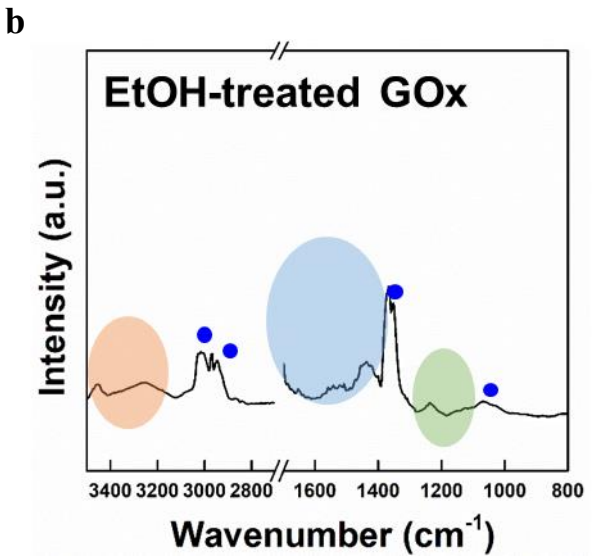


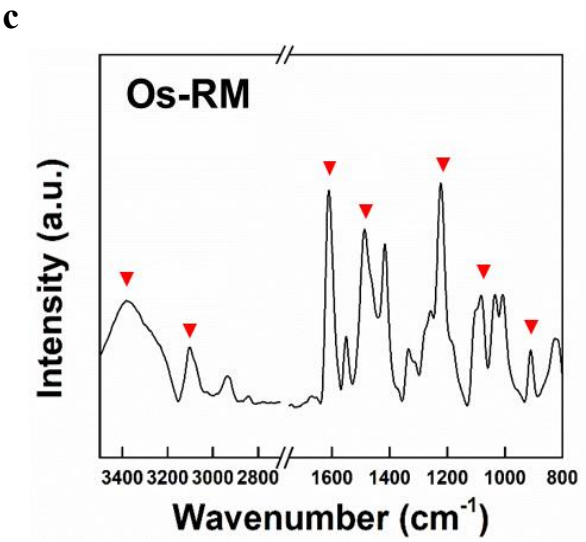


**Figure S3. FTIR spectra.** FTIR spectra of a) GOx, b) ethanol-treated GOx, c) Os-RM. The native GOx. In this case, the Os-RM layer was prepared by drop-casting onto Au-sputtered Si wafer.[S1,S2] The right panel shows a list of peak positions observed from the FTIR spectrum of native GOx.[S2] Ethanol-treated GOx were prepared by immersing them in an ethanol solution for 1 hr.

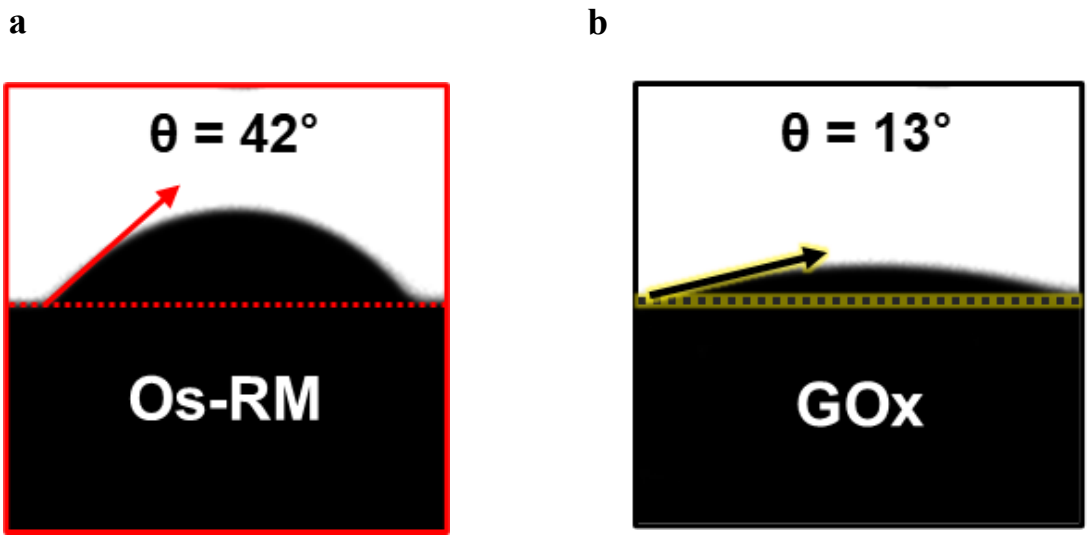


**Figure S4**. **Water contact angle.** Water contact angles of a) pristine Os-RM and b) GOx layer onto Si wafer.

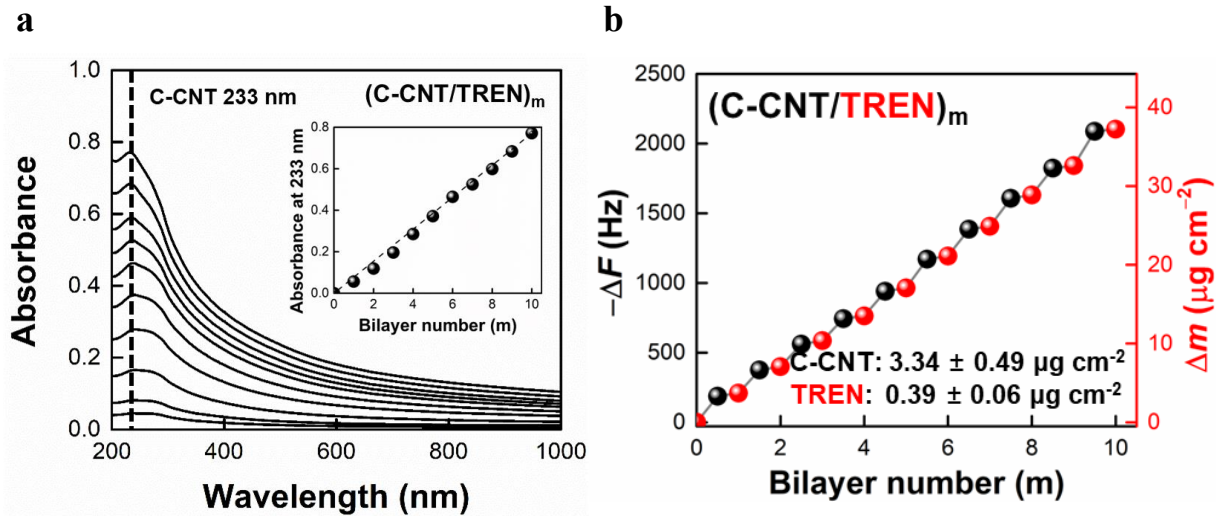


**Figure S5. Characterization of (C-CNT/TREN)$_m$ multilayers.** a) The UV-vis absorbance of the multilayers according to the increase of bilayer number (m). b) Changes in frequency (-*ΔF*) and mass (*Δm*) resulting from the adsorption of C-CNTs and TREN were observed with the rise in bilayer number (m). The mass changes were derived from the frequency changes of the C-CNTs and TREN layers adsorbed on the crystal surface. In this case, the loading amounts per C-CNT/TREN bilayer were calculated to be approximately 3.7 ± 0.5 μg cm$^{-2}$.

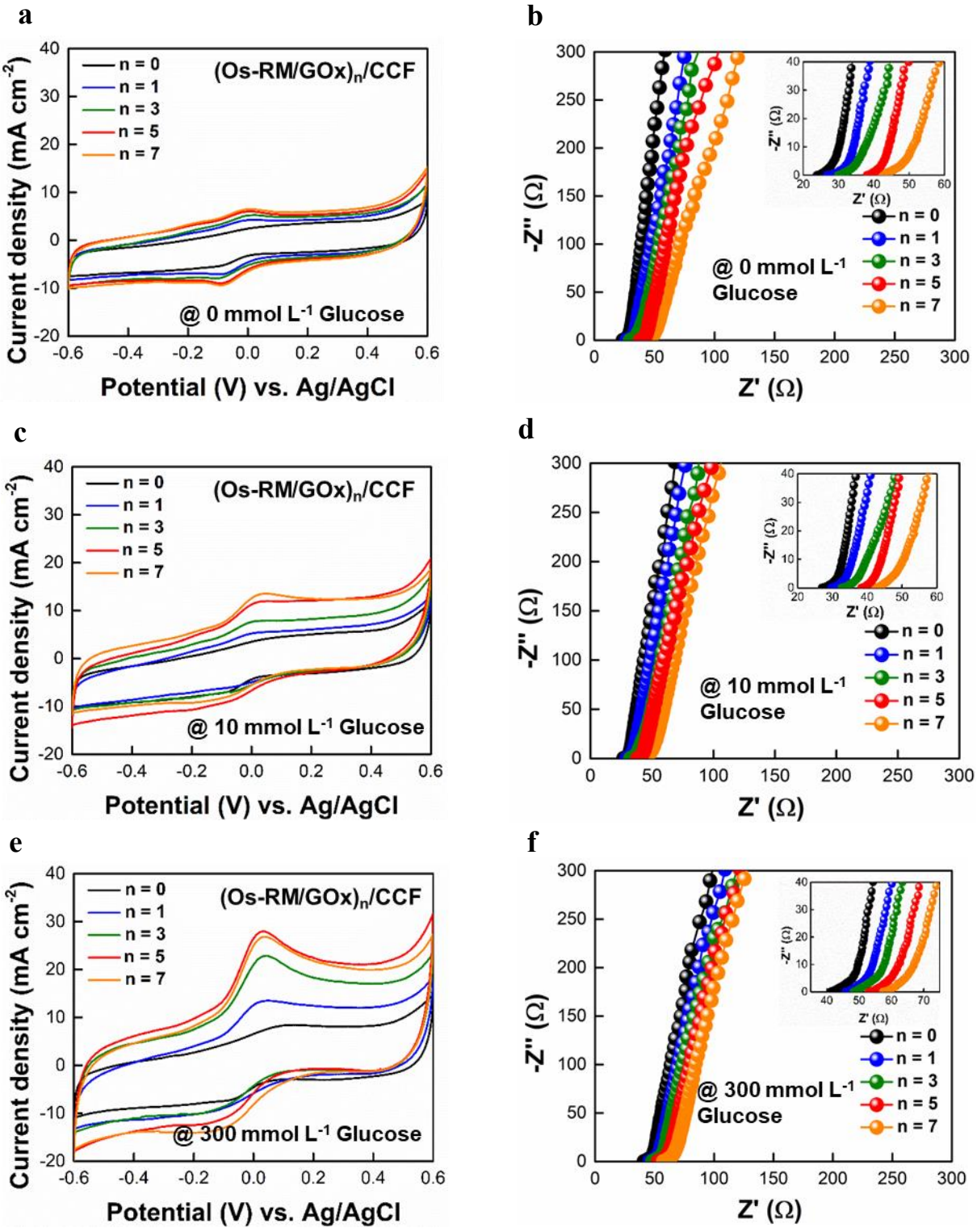


**Figure S6. Electrochemical performance of (Os-RM/GOx)$_n$/CCF.** a) CV curves and b) Nyquist plots of (Os-RM/GOx)$_n$/CCF at 0 mmol L$^{-1}$. c) CV curves and d) Nyquist plots of (Os-RM/GOx)$_n$/CCF at 10 mmol L$^{-1}$. e) CV curves and f) Nyquist plots of (Os-RM/GOx)$_n$/CCF at

300 mmol $L^{-1}$ glucose with increasing the bilayer number (n) from 0 to 7. The insets of b), d), and f) shows the Nyquist plots magnified in the high-frequency range. All measurements were performed at a scan rate of 5 mV $s^{-1}$ in PBS under ambient conditions.

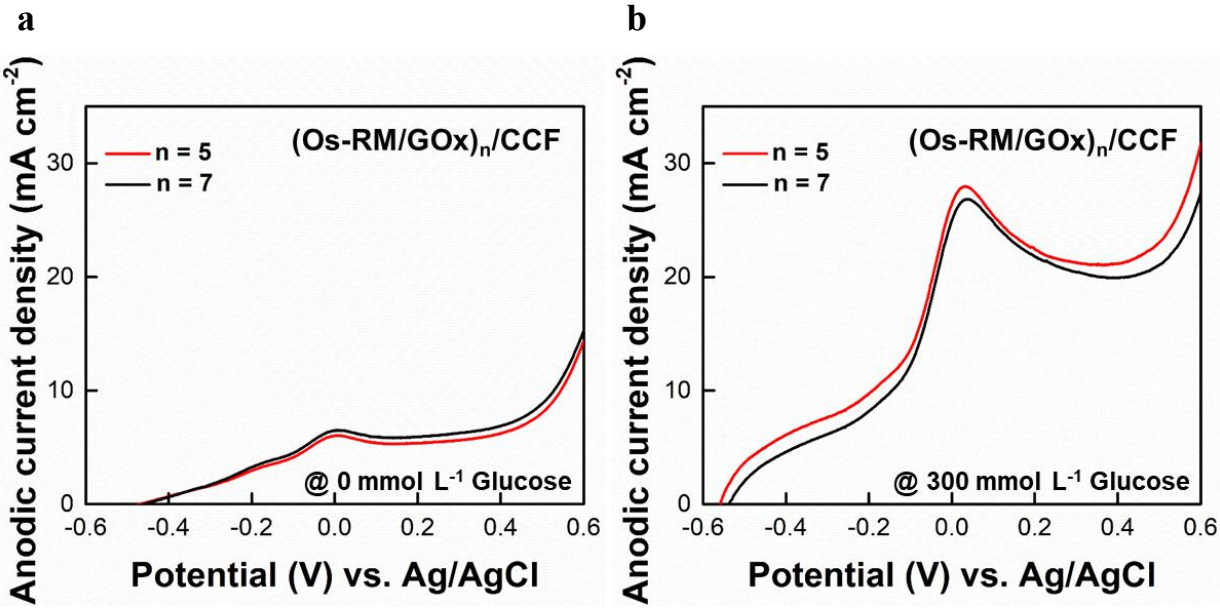


**Figure S7. Anodic current density.** Comparison of anodic current densities of (Os-RM/GOx)$_5$/CCF and (Os-RM/GOx)$_7$/CCF at a) 0 mmol L$^{-1}$ and b) 300 mmol L$^{-1}$ glucose in the PBS solution.

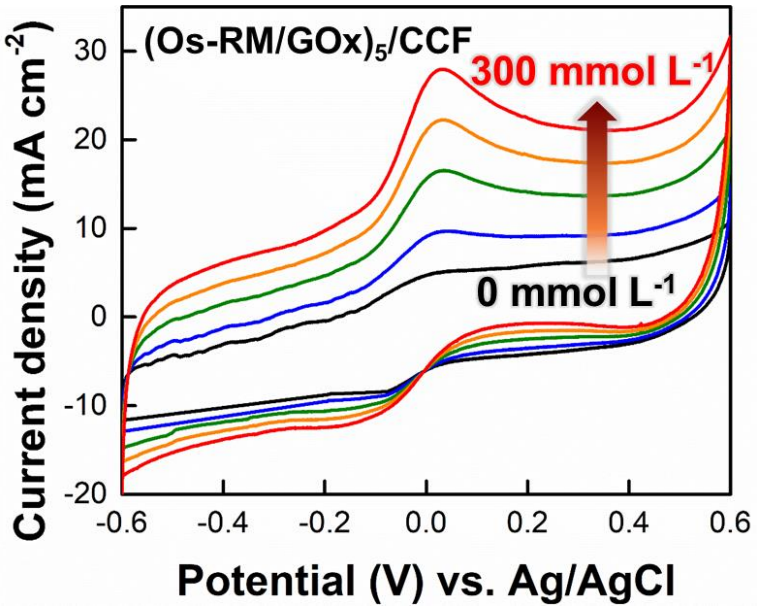


**Figure S8. CV curves.** CVs of (Os-RM/GOx)$_5$/CCF at various glucose concentrations: 0 mmol $L^{-1}$ (black color), 10 mmol $L^{-1}$ (blue color), 50 mmol $L^{-1}$ (green color), 100 mmol $L^{-1}$ (orange color), and 300 mmol $L^{-1}$ (red color).

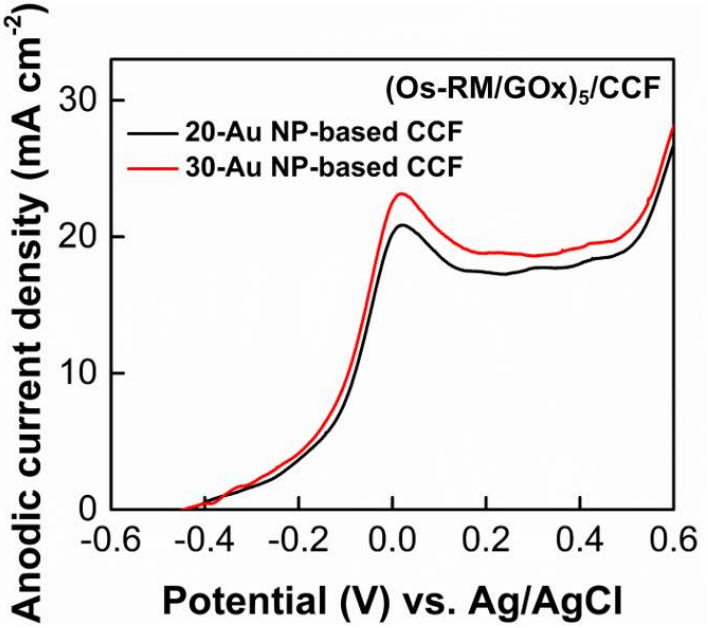


**Figure S9. Anodic current density curves of (Os-RM/GOx)$_5$/20-Au NP-based CCF and (Os-RM/GOx)$_5$/30-Au NP-based CCF.** In this case, the scan rate of 5 mV $s^{-1}$ in PBS solution containing 300 mmol $L^{-1}$ glucose at 36.5 ˚C. Also, the electrical conductivity and resistivity of the 30-Au NP/10-C-CNT/cotton fiber were measured to be approximately ~2.0 x $10^4$ S $cm^{-1}$ and a resistivity of ~4.9 x $10^{-5}$ Ω cm, respectively.

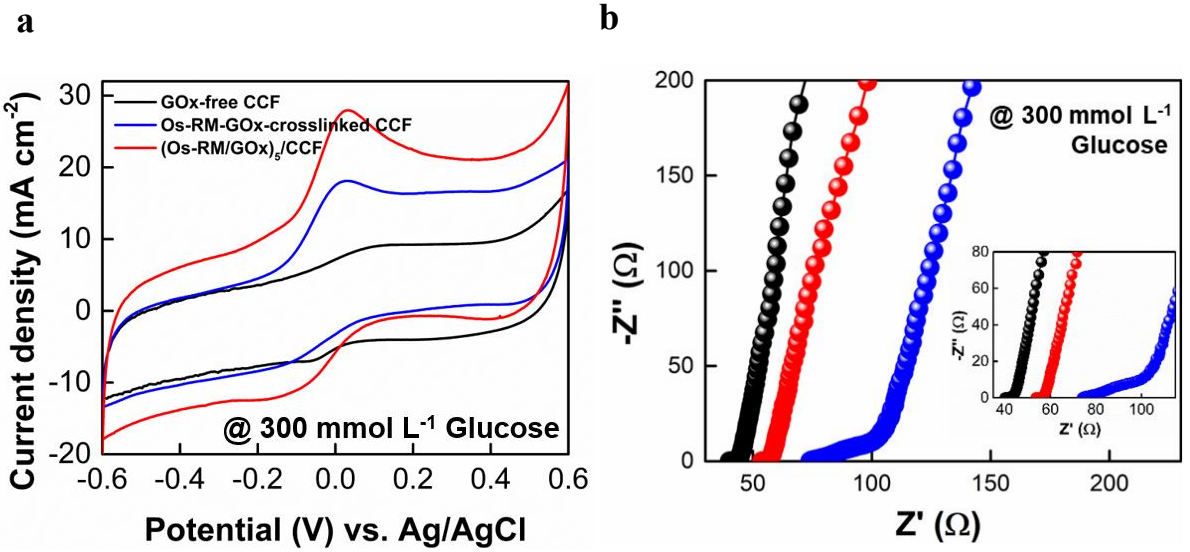


**Figure S10. Electrochemical performance of various CCF-based electrodes.** a) CVs and b) Nyquist plot of GOx-free CCF (black color), Os-RM-GOx-crosslinked CCF (blue color), and $(Os\text{-}RM/GOx)_5$/CCF (red color). These results demonstrated the effectiveness of LbL-assembled $(Os\text{-}RM/GOx)_5$/CCF with superior current density and lower resistance compared to conventional Os-RM/GOx-crosslinked CCF.[S3]

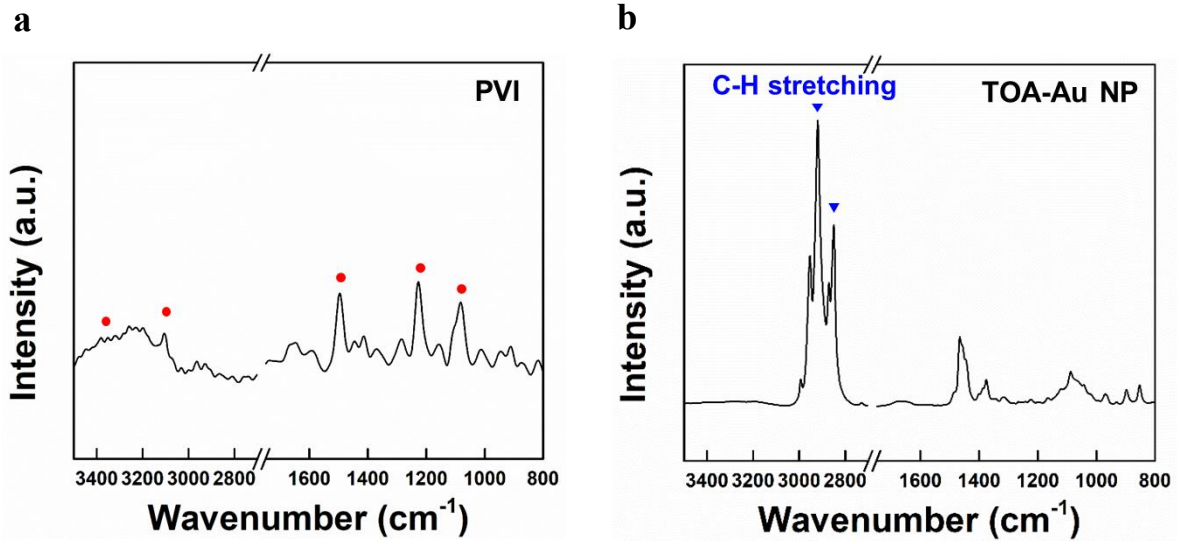


| Wavenumber ($cm^{-1}$) | Assignments |
|---|---|
| ~3397 | Bound $H_2O$ in PVI |
| 3110 | C-H vibration of the imidazole ring |
| 1499, 1230 | Imidazole group of PVI |
| 1089 | Azole C-H group in-plane bending |

**Figure S11. FTIR spectra.** FTIR spectra of a) PVI and b) TOA-Au NP. The bottom panel shows the list of peak positions observed from FTIR spectrum of PVI.

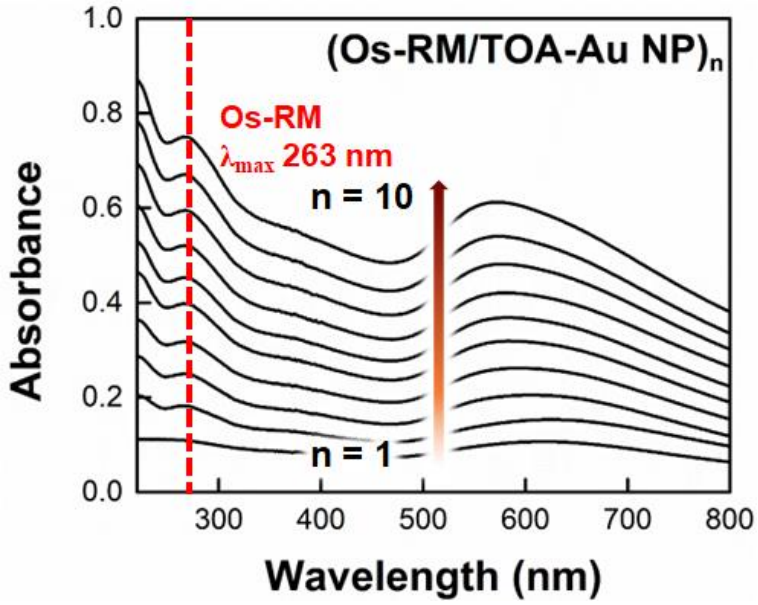


**Figure S12. UV-vis spectra.** UV-vis spectra of (Os-RM/TOA-Au NP)$_n$ multilayers as a function of bilayer number (n).

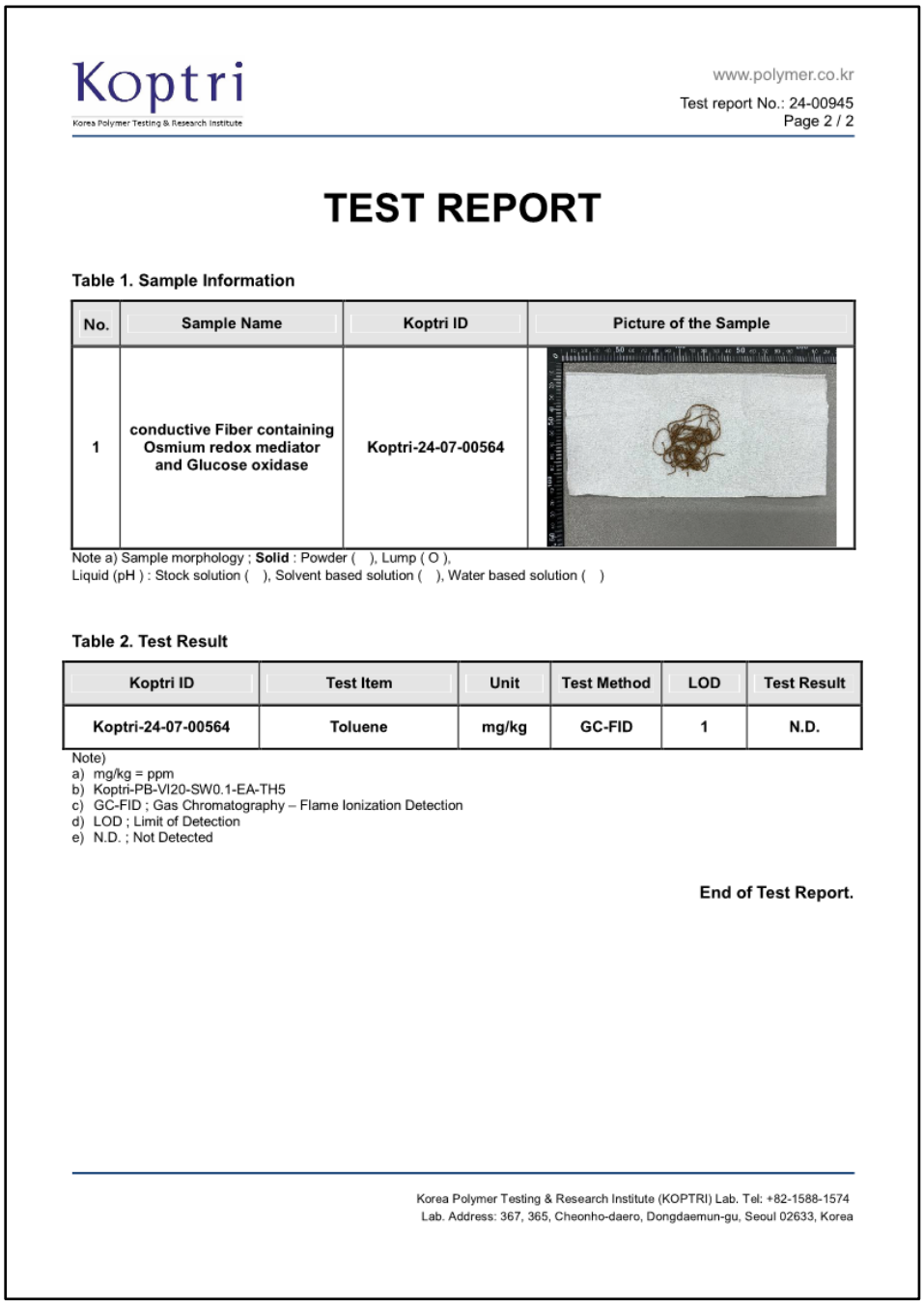

Koptri
Korea Polymer Testing & Research Institute

www.polymer.co.kr
Test report No.: 24-00945
Page 2 / 2

# TEST REPORT

**Table 1. Sample Information**

| No. | Sample Name | Koptri ID | Picture of the Sample |
|---|---|---|---|
| 1 | conductive Fiber containing Osmium redox mediator and Glucose oxidase | Koptri-24-07-00564 | |

Note a) Sample morphology ; **Solid** : Powder ( ), Lump ( O ),
Liquid (pH ) : Stock solution ( ), Solvent based solution ( ), Water based solution ( )

**Table 2. Test Result**

| Koptri ID | Test Item | Unit | Test Method | LOD | Test Result |
|---|---|---|---|---|---|
| Koptri-24-07-00564 | Toluene | mg/kg | GC-FID | 1 | N.D. |

Note)
a) mg/kg = ppm
b) Koptri-PB-VI20-SW0.1-EA-TH5
c) GC-FID ; Gas Chromatography – Flame Ionization Detection
d) LOD ; Limit of Detection
e) N.D. ; Not Detected

**End of Test Report.**

Korea Polymer Testing & Research Institute (KOPTRI) Lab. Tel: +82-1588-1574
Lab. Address: 367, 365, Cheonho-daero, Dongdaemun-gu, Seoul 02633, Korea

**Figure S13. Residual toluene quantification.** No detectable residual toluene was observed within the (Os-RM/GOx/Os-RM/TOA-Au NP)$_3$/CCF anode, which was confirmed by GC-FID (Gas Chromatography – Flame Ionization Detection) at the Korea Polymer Testing & Research Institute (KOPTRI, Seoul, Korea).

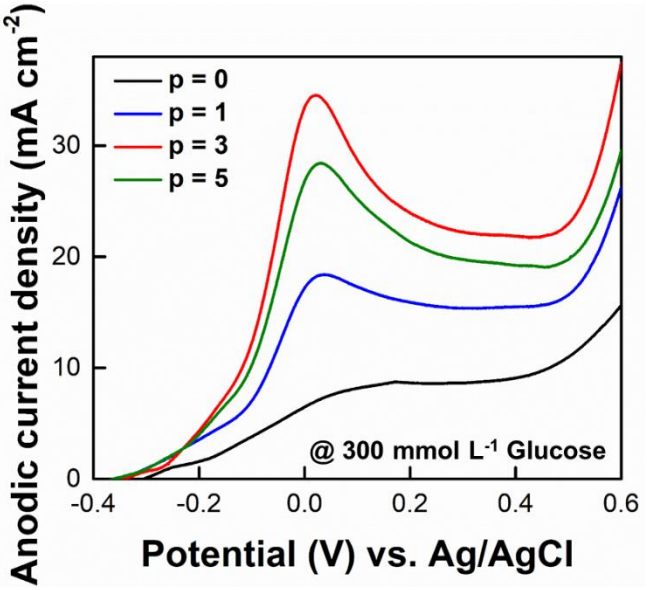


**Figure S14. Anodic current density.** Electrochemical performance of the (Os-RM/GOx/Os-RM/TOA-Au NP)$_p$ multilayer-coated CCF anode as a function of the periodic layer number (p). In this case, as the periodic number (p) of (Os-RM/GOx/Os-RM/TOA-Au NP)$_p$ multilayers increased from 0 to 5, the anodic current density of (Os-RM/GOx/Os-RM/TOA-Au NP)$_p$/CCF electrode (at 300 mmol $L^{-1}$ glucose concentration) was significnatly increased from 15.6 (for p=1) to 37.5 mA $cm^{-2}$ (for p=3), and then slighlty decreased up to 29.5 mA $cm^{-2}$ (for p=5).

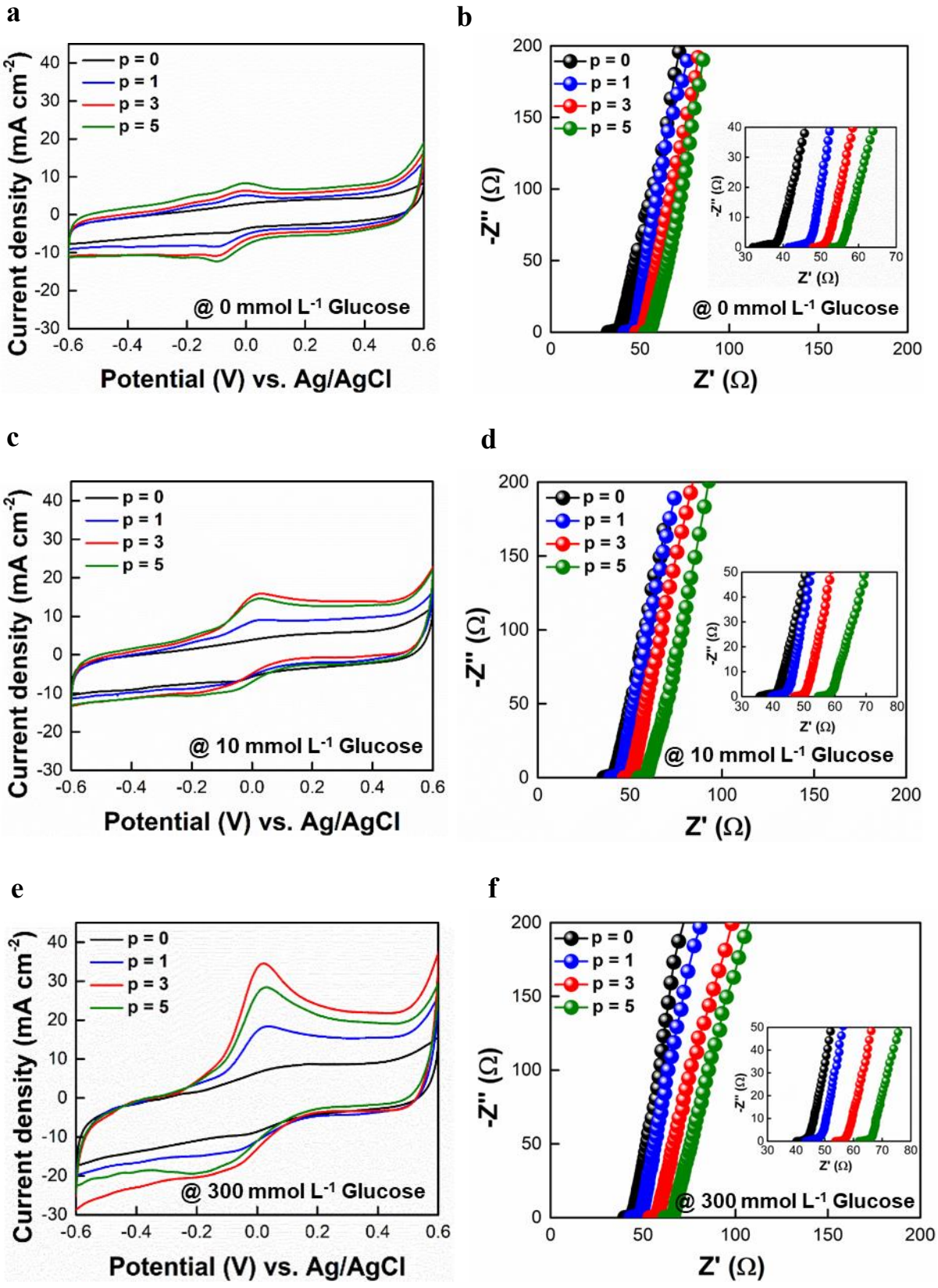
a
Current density (mA cm-2)
Potential (V) vs. Ag/AgCl
p = 0
p = 1
p = 3
p = 5
@ 0 mmol L-1 Glucose
b
-Z'' (Ω)
Z' (Ω)
p = 0
p = 1
p = 3
p = 5
@ 0 mmol L-1 Glucose
c
Current density (mA cm-2)
Potential (V) vs. Ag/AgCl
p = 0
p = 1
p = 3
p = 5
@ 10 mmol L-1 Glucose
d
-Z'' (Ω)
Z' (Ω)
p = 0
p = 1
p = 3
p = 5
@ 10 mmol L-1 Glucose
e
Current density (mA cm-2)
Potential (V) vs. Ag/AgCl
p = 0
p = 1
p = 3
p = 5
@ 300 mmol L-1 Glucose
f
-Z'' (Ω)
Z' (Ω)
p = 0
p = 1
p = 3
p = 5
@ 300 mmol L-1 Glucose

**Figure S15. Electrochemical performance.** a) CV curves and b) Nyquist plots of (Os-RM/GOx/Os-RM/TOA-Au NP)$_p$/CCF as a function of periodic layer number (p) at 0 mmol L$^{-1}$. c) CV curves and d) Nyquist plots of (Os-RM/GOx/Os-RM/TOA-Au NP)$_p$/CCF as a function of periodic layer number (p) at 10 mmol L$^{-1}$. e) CV curves and f) Nyquist plots of (Os-RM/GOx/Os-RM/TOA-Au NP)$_p$/CCF at 300 mmol L$^{-1}$ glucose. The insets of b), d), and f) shows the Nyquist plots magnified in the high-frequency range. All measurements were performed at a scan rate of 5 mV s$^{-1}$ in PBS under ambient conditions.

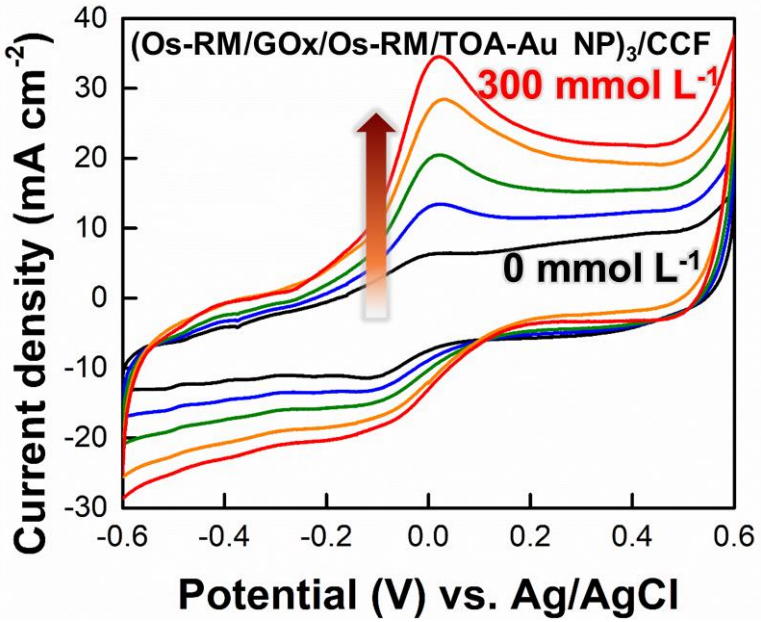


**Figure S16. Electrochemical performance.** CVs of (Os-RM/GOx/Os-RM/TOA-Au NP)$_3$/CCF with increasing the glucose concentration from 0 to 300 mmol L$^{-1}$. The CV curves show the electrochemical performance of (Os-RM/GOx/Os-RM/TOA-Au NP)$_3$/CCF, representing the changes of current densities in response to increasing the glucose concentration.

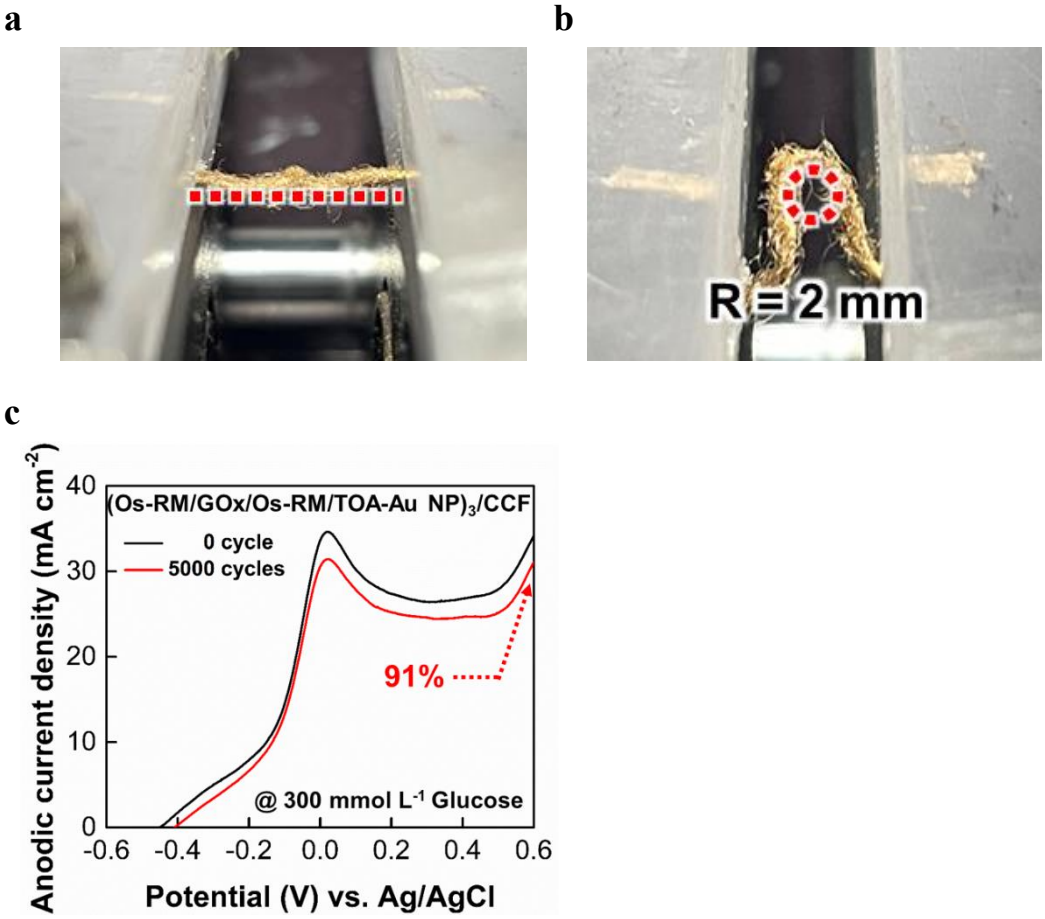


**Figure S17. Mechanical stability of hybrid BFC electrode.** a) and b) Photographic images of MET-hybrid BFC electrode on bending machine. c) Comparison of anodic current density curves of (Os-RM/GOx/Os-RM/TOA-Au NP)$_3$/CCF anode before and after 5000 bending cycles, with bending radius of about 2 mm.

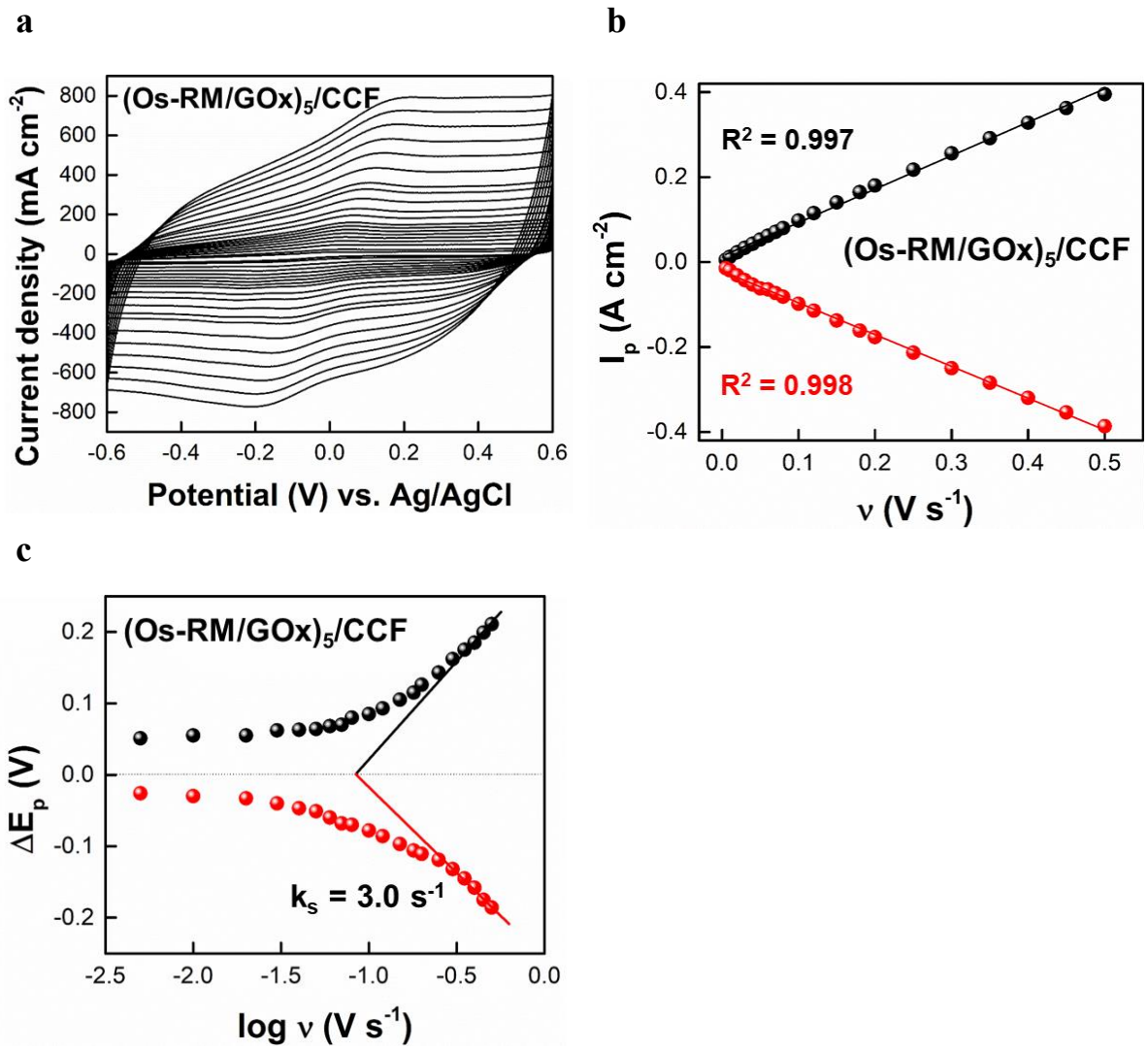


**Figure S18. Electrochemical response.** a) Scan rate-dependent CVs of $(Os\text{-}RM/GOx)_5/CCF$ in the PBS buffer solution. In this case, the scan rates (from the inner to the outer curve) of 0.005, 0.01, 0.02, 0.03, 0.04, 0.05, 0.06, 0.07, 0.08, 0.1, 0.12, 0.15, 0.18, 0.2, 0.25, 0.3, 0.35, 0.4, 0.45, and 0.5 V $s^{-1}$ were employed for electrochemical response measurements. b) Change in the peak current of $(Os\text{-}RM/GOx)_5/CCF$ with increasing the scan rate (ν) from 0.005 to 0.5 V $s^{-1}$. c) Change in potential ($E-E_0$) of $(Os\text{-}RM/GOx)_5/CCF$ as a function of log (ν).

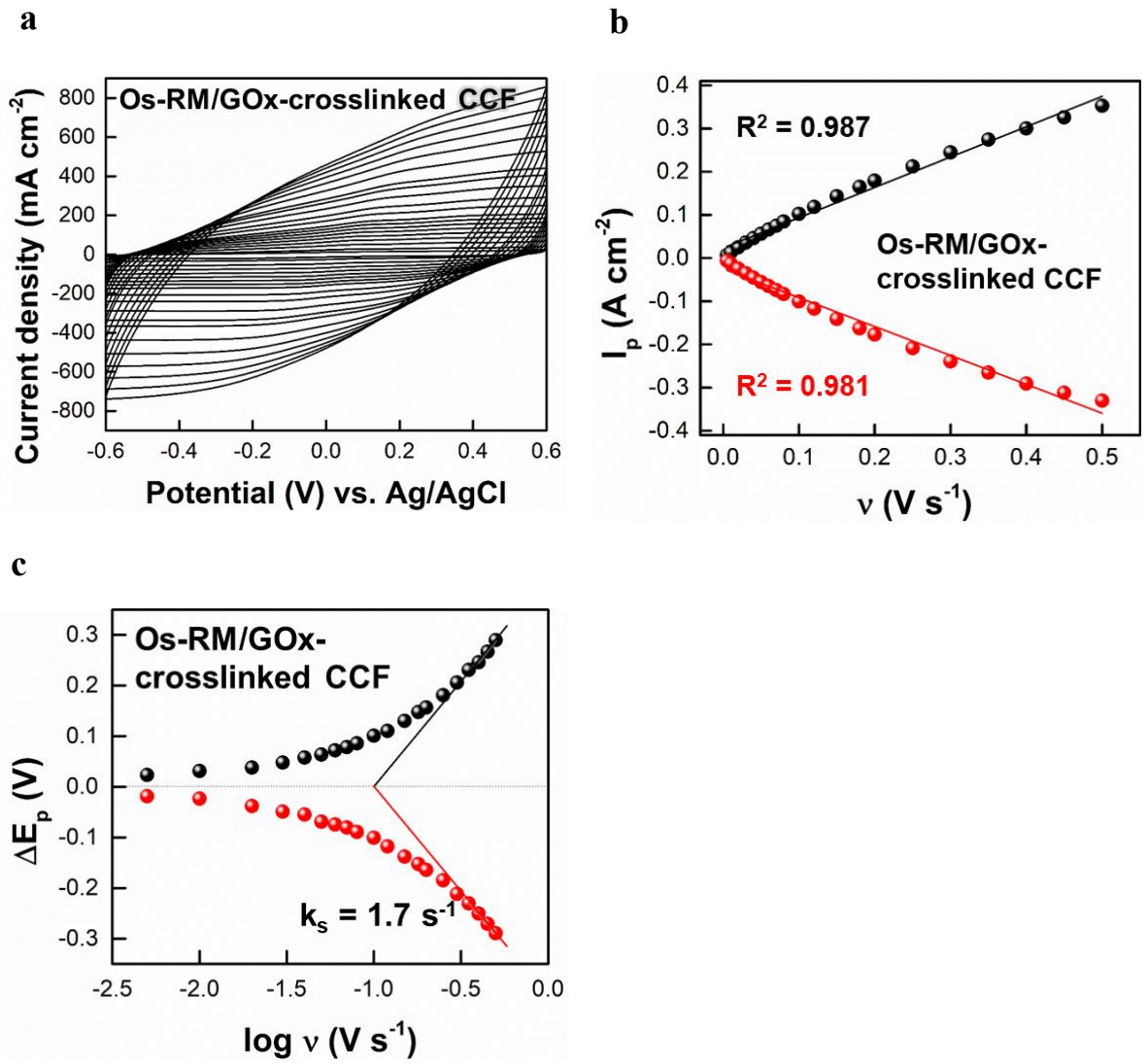


**Figure S19. Electrochemical response.** a) Scan rate-dependent CVs of Os-RM/GOx-crosslinked CCF in the PBS buffer solution. In this case, the scan rates (from the inner to the outer curve) used in **Figure S18a** were employed for electrochemical response measurements. b) Change in the peak current of Os-RM/GOx-crosslinked CCF with increasing scan rate (ν) from 0.005 to 0.5 V $s^{-1}$. c) Change in potential ($E-E_0$) of Os-RM/GOx-crosslinked CCF as a function of log (ν).

a

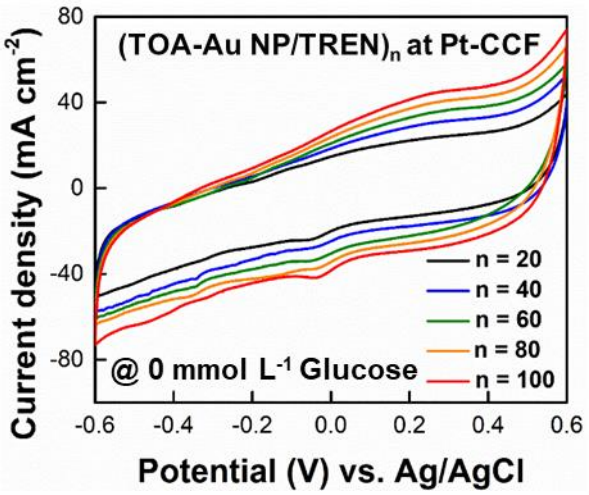
(TOA-Au NP/TREN)n at Pt-CCF
Current density (mA cm-2)
Potential (V) vs. Ag/AgCl
@ 0 mmol L-1 Glucose
n = 20
n = 40
n = 60
n = 80
n = 100

b

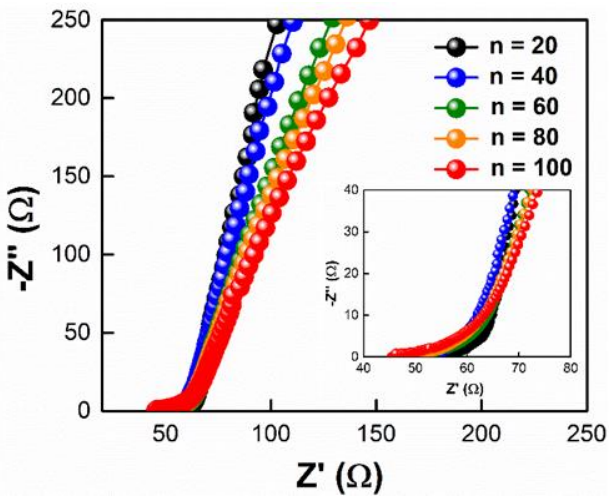
-Z'' (Ω)
Z' (Ω)
n = 20
n = 40
n = 60
n = 80
n = 100

c

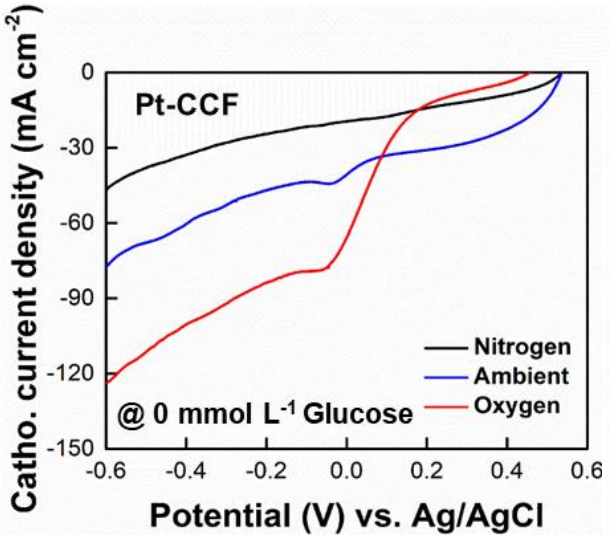
Pt-CCF
Catho. current density (mA cm-2)
Potential (V) vs. Ag/AgCl
@ 0 mmol L-1 Glucose
Nitrogen
Ambient
Oxygen

d

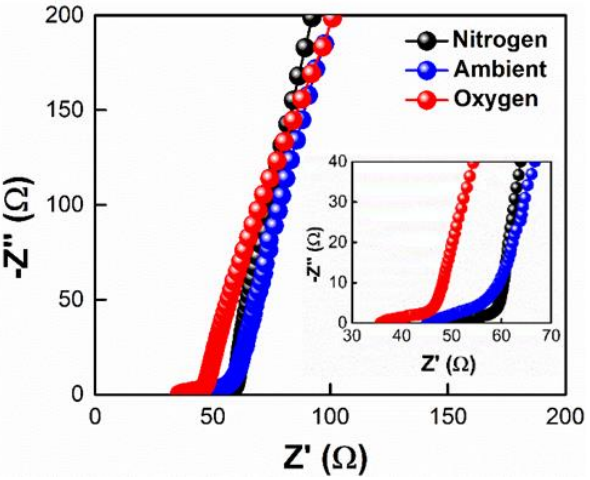
-Z'' (Ω)
Z' (Ω)
Nitrogen
Ambient
Oxygen

e

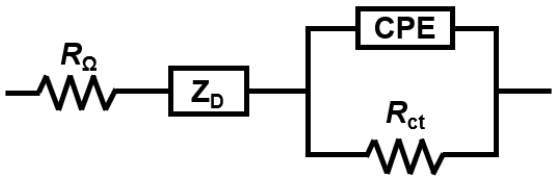
RΩ
ZD
CPE
Rct

**Figure S20. Electrochemical properties of Pt-CCF.** a) CV curves and b) Nyquist plots of the $(TOA\text{-}Au\ NP/TREN)_n$ multilayer-embedded Pt-CCF. To enhance the oxygen reduction reaction (ORR) activity in the cathode, a platinum (Pt), known for its excellent ORR activity, was sputtered onto CCF. Subsequently, we systematically controlled the number of bilayers (n) in $(TOA\text{-}Au\ NP/TREN)_n$ multilayers on the cathode, ranging from 20 to 100, to assess its influence on the power performance of CCF-hybrid BFCs. As a result, the maximum cathodic current density reached approximately −73.1 mA $cm^{-2}$ at a potential of −0.6 V for the $(TOA\text{-}Au\ NP/TREN)_{100}$ at Pt-CCF cathode. (i.e., Pt-CCF). c) CV curves and d) Nyquist plots of Pt-CCF highlight the effect of gas conditions on Pt-CCF. Furthermore, we explored the electrochemical cathodic properties of Pt-CCF in oxygen-free ($N_2$-saturated), ambient, and oxygen-rich PBS solutions. The cathodic current densities measured at −0.6 V in ambient and oxygen-rich conditions were −75.7 and −123.8 mA $cm^{-2}$, respectively. This remarkable enhancement is primarily attributed to the expanded active surface area of the fibril-structured host electrode, coupled with the uniform deposition of highly ORR-active Pt over the entire cathode. e) Equivalent electrical circuit of a Nyquist plot. These spectra were fitted using two equivalent circuits. The first consists of the cell resistance, $R_\Omega$, in series with a parallel combination of a charge transfer resistance, $R_{ct}$, and a constant phase element, CPE. The CPE is modeled as a non-ideal capacitor according to the relation $CPE = -1/(Ci\omega)^{\alpha}$, where C is the capacitance (describing the charge separation at the double layer interface), ω is the angular frequency and α is the CPE exponent (due to the non-uniformity and roughness of the surface and interfaces). A diffusion impedance element ($Z_D$) was added in series before the parallel combination, expressed by $Z_D = R_D\coth[(\tau i\omega)\ \alpha]\ (\tau i\omega)^{-\alpha}$, where $\alpha \leq 0.5$, α is the diffusion time constant and $R_D$ the diffusion resistance.

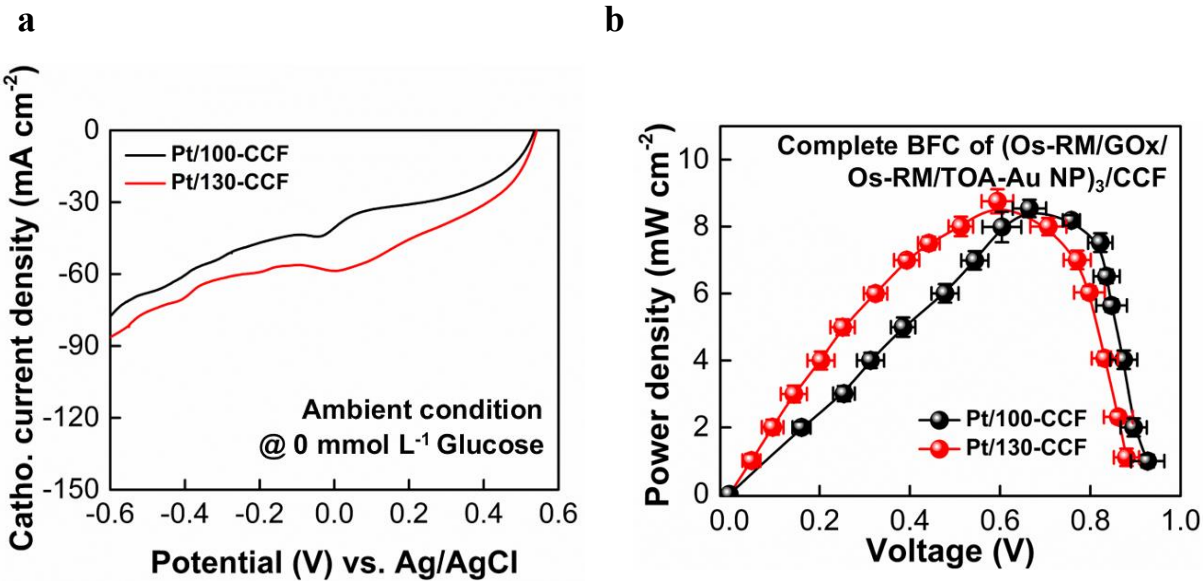


**Figure S21. Electrochemical properties.** a) CV curves of Pt/(TOA-Au NP/TREN)$_{100}$/(C-CNT/TREN)$_{10}$/cotton fiber cathode and Pt/(TOA-Au NP/TREN)$_{130}$/(C-CNT/TREN)$_{10}$/cotton fiber cathode and b) Power outputs of the complete hybrid BFCs based on Pt/(TOA-Au NP/TREN)$_{100}$/(C-CNT/TREN)$_{10}$/cotton fiber cathode and Pt/(TOA-Au NP/TREN)$_{130}$/(C-CNT/TREN)$_{10}$/cotton fiber cathode. In this case, the anode was fixed at the (Os-RM/GOx/Os-RM/TOA-Au NP)$_3$/CCF.

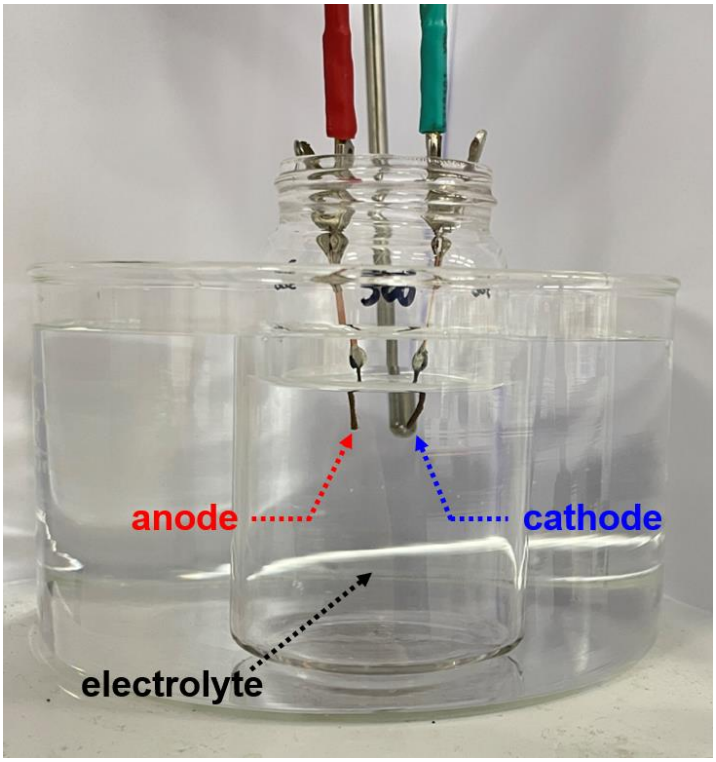


**Figure S22**. **Photographic image of MET-hybrid BFC.** It is composed of (Os-RM/GOx/Os-RM/TOA-Au NP)$_3$/CCF anode and Pt/(TOA-Au NP/TREN)$_{100}$/(C-CNT/TREN)$_{10}$/cotton fiber cathode.

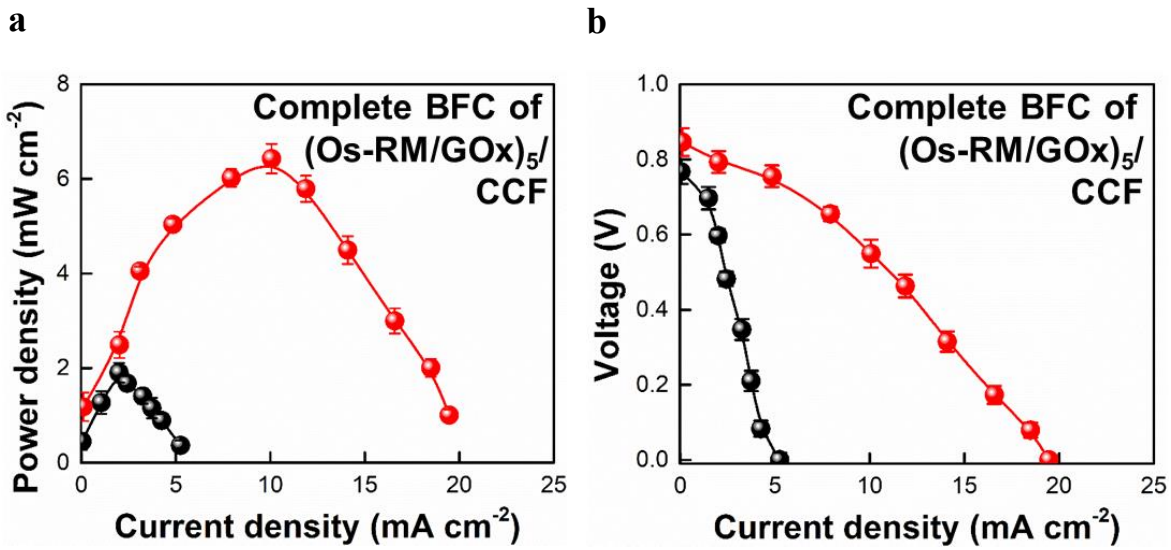


**Figure S23. External load-dependent power output profiles of the complete hybrid BFC.** a) Power (P) – current (I) profiles, and b) Voltage (V) – current (I) profiles of the (Os-RM/GOx)$_5$/CCF in PBS solution containing 10 mmol L$^{-1}$ (black color) and 300 mmol L$^{-1}$ glucose (red color).

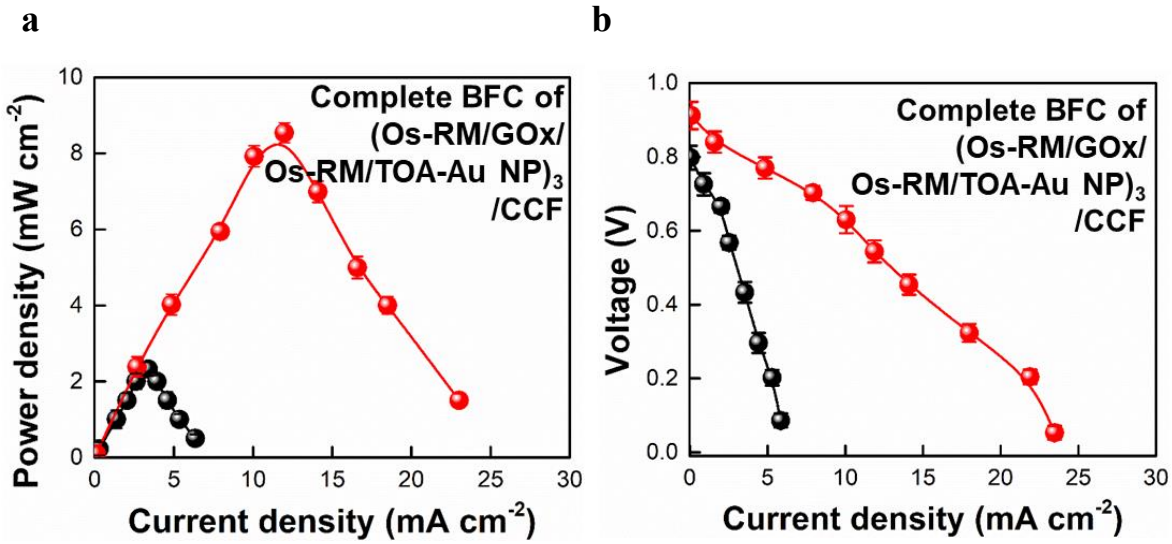


**Figure S24. External load-dependent power output profiles of the complete hybrid BFC.** a) Power (P) – current (I) profiles, and b) Voltage (V)–current (I) profiles of (Os-RM/GOx/Os-RM/TOA-Au NP)$_3$/CCF in PBS solutions containing 10 mmol $L^{-1}$ (black color) and 300 mmol $L^{-1}$ glucose (red color).

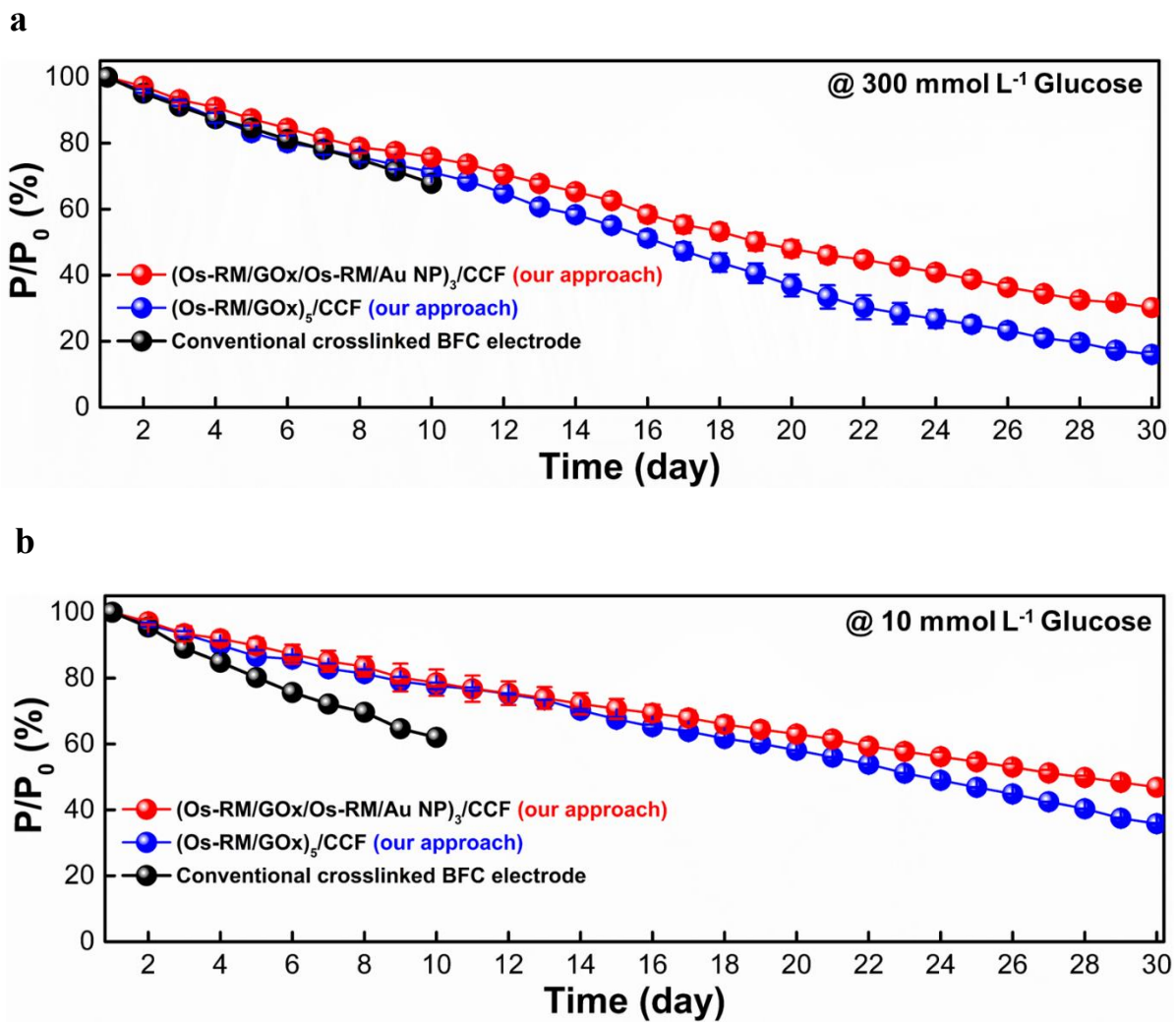


**Figure S25. Relative power retention of CCF-based complete hybrid BFCs.** Power retention of the complete hybrid BFCs of conventional crosslinked BFC electrode (black color), $(Os\text{-}RM/GOx)_5$/CCF (blue color, our approach), $(Os\text{-}RM/GOx/Os\text{-}RM/TOA\text{-}Au\ NP)_3$/CCF (red color, our approach) in PBS solutions containing a) 300 mmol $L^{-1}$ and b) 10 mmol $L^{-1}$ glucose at 36.5 °C.

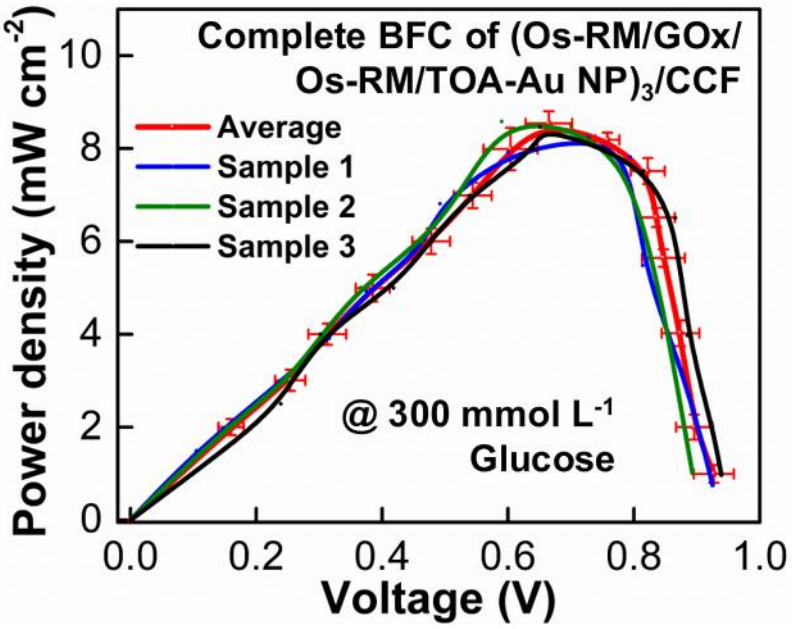


**Figure S26. The consistency of the complete hybrid BFC samples.** Power output of the complete hybrid BFCs of (Os-RM/GOx/Os-RM/TOA-Au NP)$_3$/CCF (in PBS solutions containing 300 mmol $L^{-1}$ glucose at 36.5 °C. No significant disparities were observed in the power output characteristics of the three samples.

**Table S1.** Power output and stability of various single fibrous MET-hybrid BFCs reported to date.

| Anode | Cathode | OCV (V) | Max. Power density (mW cm$^{-2}$) | Power Stability (Time span) | Ref. |
|---|---|---|---|---|---|
| **(Os-RM/GOx/ Os-RM/TOA-Au NP)$_3$/CCF** | **Pt/CCF** | **0.92** | **8.5** | **80% (10 days) 47% (1 month)** | **This work** |
| GOx/ RM1/MWCNT/BY | BOD/RM2/MWCNT/BY | 0.70 | 1.5 | 76% (48 hours) | S3 |
| LOD+BSA/1,4-NQ/BP | BOD/PPIX/CNT/BP | 0.74 | 0.5 | 84% (48 hours) | S4 |
| FAD-GDH/Os(dmb)PVI/EPD-MWCNTs | Lac/Os(bpy)PVI/EPD-MWCNTs | 0.59 | 0.4 | 56% (7 days) | S5 |
| LOD/PVI-[Os(bpy)$_2$Cl]/CNT/Fiber | BOD/CNT/PTFE-CNT/Fiber | 0.6 | 0.3 | 80% (12 hours) | S6 |
| GOx/CC | Prussian Blue/CC | 0.38 | 0.1 | 68% (4 hours) | S7 |
| PDA-MPC/GOx/TTF/CNT Fiber | PDA-MPC/Pt/C/CNT Fiber | 0.4 | 0.03 | 92% (6 hours) | S8 |

OCV: Open circuit voltage, CCF: conductive cotton fiber, BY: biscrolled yarn, BP: bucky paper, CC: carbon cloth
GOx: glucose oxidase, LOD: lactate oxidase, BOD: bilirubin oxidase, FAD-GDH: FAD-dependent glucose dehydrogenase Lac: laccase
Os-RM: poly(N-vinylimidazole)-[Os(4,4'-dimethoxy-2,2'-bipyridine)$_2$Cl])$^{+/2+}$, RM1: poly(N-vinylimidazole)-[Os(4,4'-dimethoxy-2,2'-bipyridine)$_2$Cl])$^{+/2+}$, RM2: poly(acryl amide)-poly(N-vinylimidazole)-[Os(4,4'-dichloro-2,2'-bipyridine)$_2$])$^{+/2+}$, BSA: bovine serum, 1,4-NQ: 1,4-naphthoquinone, PPIX: protoporphyrin IX, Os(dmb)PVI: [Os(4,4′-dimethyl-2,2′-bipyridine)$_2$(poly-vinylimidazole)$_{10}$Cl], Os(bpy)PVI: [Os(2,2′-bipyridine)$_2$(poly-vinylimidazole)$_{10}$Cl]$^+$, EPD: electrophoretic deposition, PTFE: Poly(tetrafluoroethylene), PDA-MPC: hydrophilic zwitterionic polydopamine-2-methacryloyloxyethyl phosphorylcholine, TTF: tetrathiafulvalene

## References

[S1] Q. Wang, X. Zhang, L. Huang, Z. Zhang, S. Dong, *Angew. Chem. Int. Ed.* **2017**, *56*, 16082.

[S2] M. Portaccio, B. D. Ventura, D. G. Mita, N. Manolova, O. Stoilova, I. Rashkov, M. Lepore, *J. Sol-Gel Sci. Technol.* **2011**, *57*, 204.

[S3] C. H. Kwon, S.-H. Lee, Y.-B. Choi, J. A. Lee, S. H. Kim, H.-H. Kim, G. M. Spinks, G. G. Wallace, M. D. Lima, M. E. Kozlov, R. H. Baughman, S. J. Kim, *Nat. Commun.* **2014**, 5, 3928.

[S4] X. Chen, L. Yin, J. Lv, A. J. Gross, M. Le, N. G. Gutierrez, Y. Li, I. Jeerapan, F. Giroud, A. Berezovska, R. K. O. Reilly, S. Xu, S. Cosnier, J. Wang, *Adv. Funct. Mater.* **2019**, *29*, 1905785.

[S5] Z. Zhong, L. Qian, Y. Tan, G. Wang, L. Yang, C. Hou, A. Liu, *J. Electroanal. Chem.* **2018**, *823*, 723.

[S6] S. Yin, X. Liu, T. Kaji, Y. Nishina, T. Miyake, *Biosens. Bioelectron.* **2021**, *179*, 113107.

[S7] C. Wang, E. Shim, H.-K. Chang, N. Lee, H. R. Kim, J. Park, *Biosens. Bioelectron.* **2020**, *169*, 112652.

[S8] Y. Guo, C. Chen, J. Feng, L. Wang, J. Wang, C. Tang, X. Sun, H. Peng, *Small Methods* **2022**, *6*, 2200142.